Effect of chromium doping on structural and dielectric properties of $Sr_{1-x}Cr_xZn_2Fe_4O_{11}$ hexagonal ferrites

A. D. Khalid [a], H. M. Khan [b], M.T. Khan [b], M. I. Khan [c], M. Sharif [d], I. U. Khawja [e], M. Yosif [b], M. N. Khan [f], S. M. El-Bahy [g], M. S. Hasan [h*], M. Awais [h]

[a] *University Institute of Radiological Sciences and Medical Imaging Technology, The University of Lahore, Lahore Pakistan*
[b] *Institute of Physics, The Islamia university of Bahawalpur, Pakistan*
[c] *Department of Physics, the University of Lahore, Lahore Pakistan.*
[d] *Department of DNA and Serology Punjab Forensic Science Agency, Lahore Pakistan*
[e] *Department of Physics, Hazara University Mansehra, kpk, Pakistan*
[f] *Department of Physics, Faculty of Science, Islamic University of Madinah, Madinah, 42351, Saudi Arabia*
[g] *Department of Chemistry, Turabah University College, Taif University, P.O. Box 11099, Taif 21944, Saudi Arabia*
[h] *Institute of Functional Nano & Soft Materials (FUNSOM), Jiangsu Key Laboratory for Carbon-Based Functional Materials & Devices, Soochow University, Suzhou, People's Republic of China*

The R-type hexagonal ferrites $Sr_{1-x}Cr_xZn_2Fe_4O_{11}$ based on $Sr^{2+}$with configuration (x = 0.0, 0.02, 0.06, 0.1) were synthesized using the sol-gel method and sintered at 1173 K. X-ray diffraction (XRD) analysis confirmed the formation of single-phase R-type hexagonal ferrites. The substitution of Cr^{2+} affected various properties, including the lattice parameters (a (Å), c (Å)), crystallite size (nm), X-ray density (g/cm³), and unit cell volume (V (Å³)). The crystallite size of all the samples ranged from 24 nm to 37 nm. Fourier transform infrared (FTIR) spectra exhibited bands between 400 cm^{-1} and 480 cm^{-1}. The dielectric constant increased with Cr^{2+} substitution but decreased with increasing frequency. AC conductivity also increased as frequency rose. These materials are suggested for use in microwave absorption applications and transformers, as they could help enhance performance by minimizing eddy currents.

(Received February 25, 2025; Accepted August 4, 2025)

Keywords: Ferrites, Dielectric, Conductivity, Eddy current

1. Introduction

In the last decades, the researchers have increased their focus on the ferrites due to their unique properties than their bulk complements such as electrical, optical and dielectric properties. Among these ferrites the hexagonal ferrites have the most remarkable and innovative properties. These hexa ferrites properties can also be modify by modifying their synthesis techniques, sintered temperature and method of doping which can change their structural, optical, magnetic and dielectric properties [1, 2, 3]. The hexagonal ferrites have durable chemical stability, high coercively and saturation, low density sensors, microwave filters, high frequency applications telecommunication devices and radar [4,5]. Their electrical and dielectric properties are focused due to their extraordinary dielectric losses and electrical resistivity [6,7]. The ferrites are divided in four types' spinel, garnets, orthoferrites and hexagonal ferrites depending on their crystal structural. In 1952, the hexagonal ferrites were described firstly [8]. Hexagonal ferrites have

* Corresponding author: sajjad@suda.edu.cn
https://doi.org/10.15251/JOR.2025.214.463

multiplicity of crystal shapes; there are seven distinctive types of due to their chemical and crystal structures. These types are M, Y, X, Z, U and R hexagonal ferrites. [9,10]. The hexagonal ferrites base on R-type are remarkable for the researchers and scientists [11]. The reason of their popularity is owing to their usage in greater rate dielectric resonators, sensors and switches [12]. These R typed hexagonal ferrites are indicated by letter "R" it can be mounded in RR*, with the rotation of 180^0alongside the c axis and ne showed with R* letter. The frustrated crystal structure of R- hexa ferrites creates the magnetic disorder [13,14]. The influence of divalent and trivalent ions has capacity for alteration the features of R- hexaferrites in the interstitial sites of the crystal lattices. The different constraints including the particle size, composition, crystallinity and site tenancy highly affect the structural, magnetic and dielectric characteristics of the R- typed hexagonal ferrites [15,16]. In our research we synthesis the R-typed hexagonal ferrites $Sr_{1-x}Cr_xZn_2Fe_4O_{11}$based on $Sr^{2+}$with mixture (x = 0.0, 0.02, 0.06, 0.1) and their properties such as electrical, structural and dielectric were examined by influence ofCr^{2+} with different concentrations. Tehmina Amjad et al. Synthesized R-Typed hexagonal ferrites $Mn_2Ni_xFe_4O_{11}$ with various compositions ($x = 0, 0.1, 0.2, 0.3$) using the sol gel auto combustion process. They improved dielectric parameters of the models by influence of Ni^{2+} indicate their suitability for high-frequency applications [17].Sajjad Hussain et al. synthesized R-typed hexagonal ferrites based on $Sr^{2+,}$ specifically $Sr_{1-x}Mg_xSn_2Fe_4O_{11}$, with varying compositions ($x = 0.0, 0.1, 0.2, 0.3$) using the sol gel technique. They reported that these R-typed ferrites may be effective by influence of Mg^{2+} for dropping the eddy current loss which is useful for microwave absorbing devices as the electrical resistivity of the synthesized sample indicated a significant resistive character [18].Mishal Idrees et al. created R-typed hexagonal ferrites$Mg_xFe_{4-y}Yb_yMn_2O_{11}$ using the sol gel method. They concluded that as the frequency increased by influence of substituting Mg^{2+} and Yb^{3+} ions. There was an observed elevation in the alternating current (AC) conductivity. Electrical resistivity exhibited variations based on the substitution of Mg and Yb ions. Additionally, all concentration levels of the polarization against electric field (P-E) loops showed hysteresis behavior, indicating a nonlinear response in these materials [19]. Muhammad Shehbaz et al. synthesis R-type hexagonal ferrites, $Pr_xMn_2Fe_4O_{11}$, with rare earth Pr^{3+} element substitution by the sol gel technique. They reported that the samples' electrical resistivity underwent noticeable changes targeted at all of the models, the dielectric constant dropped at higher frequency. Super paramagnetic properties were present in the ultimate two meditations (x = 0.06 and 0.1) [20]. Different methods are used for the synthesis of nanomaterial [21-26]. The sol gel process is used here to fabrication the nanomaterial. It is a highly efficient and cost-effective technique for synthesizing advanced materials, particularly nanomaterial. It offers precise control over composition, particle size, and morphology, making it ideal for creating materials with tailored properties. Moreover, the process requires relatively low temperatures and shorter synthesis times, reducing energy consumption and costs [27, 28]. This work introduces the novel substitution of Sr^{2+} with Cr^{2+} in R-typed hexagonal ferrites $Sr_{1-x}Cr_xZn_2Fe_4O_{11}$ fabricated via the sol-gel method. The Cr^{2+} substitution led to significant alterations in parameters of electrical, structural, and dielectric, including enhanced dielectric constants and enhanced AC conductivity with higher frequency. The study uniquely highlights the potential of Cr^{2+}-doped ferrites in reducing eddy currents, making them highly suitable for microwave absorption devices and transformer applications. This innovative approach expands the understanding of R-type ferrites with optimization for higher frequency uses.

2. Experimental techniques

Preparing the sample of $Sr_{1-x}Cr_xZn_2Fe_4O_{11}$ with x values of 0.00, 0.02, 0.06, and 0.1 was accomplished using the sol gel auto combustion technique. The stoichiometric amounts of the respective nitrates were employed, with citric acid serving as the combustion catalyst. The procedure began by dissolving the citric acid and nitrates at equal molar ratio 1:1 in the distilled water, utilizing magnetic stirrer to achieve dissolution. The ammonia solution was introduced drop by drop in the mixture to maintain PH level 7. Following approximately one hour of continuous

stirring, a dry gel was formed at100°C temperature. The stirring was stopped when dry gel was prepared, and then gel was animated till the final product was achieved through auto-combustion. The resulting product was then ground for thirty minutes to refine the prepared samples. Subsequently, the powders were subjected to sintering in a furnace at temperature of 800°C for eight hours. Various analytical techniques were subsequently applied to characterize the synthesized ferrites.

3. Results and discussion

3.1. Structural study

The XRD displays of $Sr_{1-x}Cr_xZn_2Fe_4O_{11}$ (X = 0.00, 0.02, 0.06, 0.1) are revealed in Figure 1, confirming the successful synthesis of single phased R-type hexa ferrites. The diffraction patterns exhibit sharp, well-defined peaks, indicating high crystallinity. The most prominent reflection is observed at 2θ =31.4◦, consistent with reported values in the literature [JCPDS, card number 01-072-1243]. The XRD analysis reveals eight significant peaks at 2θ values of 25.28°, 28.43°, 31.41°, 33.89°, 37.18°, 43.07°, 48.07° and 61.82° degrees, corresponding to the crystallographic planes (004), (103), (110), (112), (105), (106), (211), and (304) of R-Type Hexaferrites structure. A noticeable change in the peakloci and a reduction in peak intensities are detected with Cr^{+2}substitutions. These changes are recognized to the alteration in ionic radii among Sr^{2+} and Cr^{2+} ions, which affects the lattice parameters. The most intense peak, corresponding to the (110) plane, is used to calculate critical crystallographic parameters, including inter-planar spacing (d), lattice constant (a), crystallite size (D) & X-ray density ($d_{x\text{-}ray}$). The systematic variation in these parameters with Cr doping confirms the structural modification of the R-type hexaferrites, producing them potential applicants for dielectric usages at higher frequency.

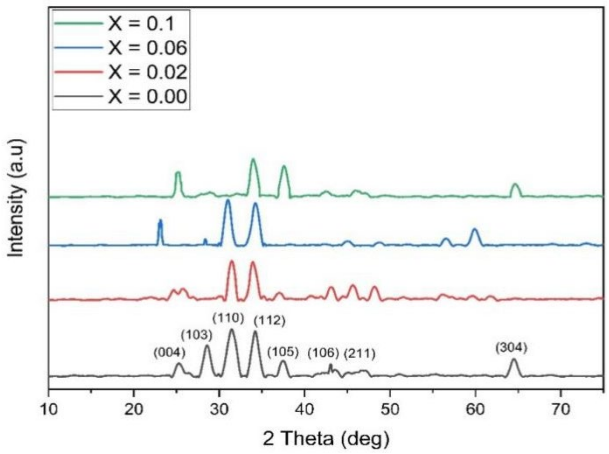

Fig. 1. XRD sketches of $Sr_{1-x}Cr_xZn_2Fe_4O_{11}(x = 0.00 - 1.0)$ *R-typed hexaferrites.*

The determination of crystalline size of the prepared models was carried out by the Debye-Scherer method [29], which is expressed as:

$$D = \frac{k\lambda}{\beta \cos\theta} \quad (1)$$

In the given formula, the constant (k) has a fixed value of 0.94, (λ) is the wavelength of the X-rays, having value of 1.54 Å (angstroms), (β) denotes the Full Width Half Maxima (FWHM) defining the peaks 'width at half of their full intensity, and (θ) corresponds to Bragg angle in X-

rays [30]. Within the sample, the determination of dislocation density employed the following formula:

$$\rho = \frac{1}{D^2} \text{ (lines/m}^2\text{)} \quad (2)$$

The resulting dislocation density values (ρ) have been provided in Table 1. There is evident that dislocation density and crystallite size are inversely proportional to each other across all Cr-substituted R-type hexaferrites [31].

Table 1. Comparison of value of crystallite size (D), and dislocation density (ρ), Inter planner spacing (d), lattice constant (a) and lattice constant c with x.

Concentration (X)	**D (nm)**	P (A°)	**d (A°)**	**a (A°)**	**c (A°)**
0.00	7.00	0.02038	0.2879	5.758	13.77
0.02	10.76	0.00863	0.28965	5.793	13.468
0.06	11.03	0.00821	0.2908	5.816	13.571
0.1	11.56	0.00748	0.28195	5.639	13.746

as in accordance with the literature [32]. It shows that the dislocation density and crystalline size are related with inverse to each other, by decreasing the dislocation density increases the crystalline size

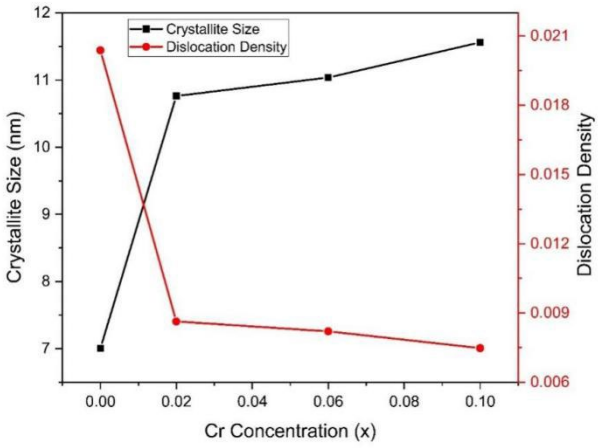

Fig. 2. Variations in dislocation density and crystalline size as a role of concentration(x).

Figure 2 denotes the variant of the particle size 'D' with certain regularity with Cr concentration (x). The prepared $Sr_{1-x}Cr_xZn_2Fe_4O_{11}$ (X = 0.00,0.02,0.06,.0.1) R-TypedHexaferriteshave crystalline size from 7.00 nm – 11.56 nm. It was observed that particles size increases in a linear way. It's also owing to the added of Cr cations for Sr cations on the lattice site [33]. The interplanar distance is typically measured as the distance between parallel crystallographic planes, such as the distance between two adjacent atomic planes in a crystal lattice. This distance is often represented by the symbol "d". Within the crystalline sample, the determination of Inter Planner Spacing employed the following formula [34]. Table 1 represents their values.

$$\frac{1}{d} = \frac{4}{3}\left(\frac{h^2+hk+k^2}{a^2}\right) + \frac{l^2}{k^2} \quad (3)$$

where, d = Inter Planner Spacing, h = Miller Indices at x side, k = Miller Indices at y side, l = Miller Indices at z side and a and c = Lattice Constant

The lattice constants were estimated using cell software and were roughly identical to previously reported values for R-type structures. The lattice constants "a" and "c" obey Vegard's law and exhibit a decreasing tendency as the ratio of substituted cations increases and are given in Table 1. It was discovered that changing the doping ratio induced a change in the intensity of the (110).

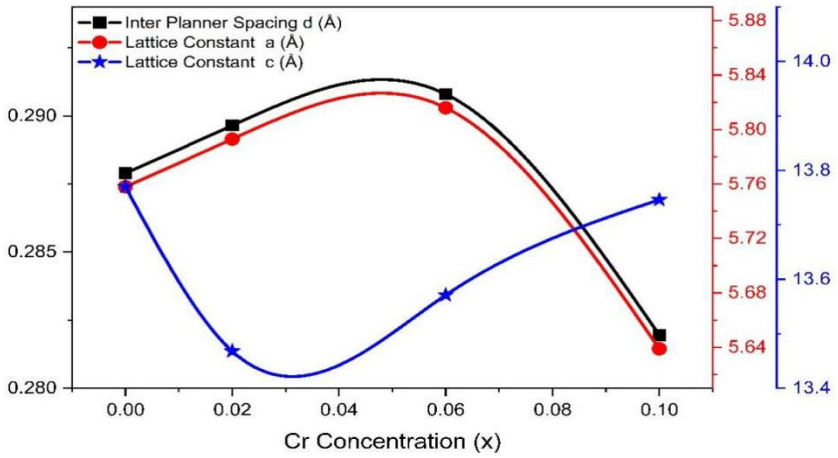

Fig. 3. Variation of Inter Planner Spacing (d), lattice constant (a) and Lattice Constant (c) (Å) by concentration x.

Based on the provided graphs it reflects that both lattice constant “a” and the interplanar spacing exhibit an increase as the concentration of Cr doping rises, reaching a peak around x = 0.06. Subsequently, these values start to decline. This way can be qualified to the feature that at lower concentrations of Chromium, the element does not effectively integrate into the crystal lattice but instead remains as an impurity along the grain boundaries. However, as the doping concentration increases sufficiently, Chromium begins to diffuse into crystal lattice, essential towards a reduction in the lattice constant "a" and interplanar spacing [35, 36].

Different metal ion properties were to blame for alteration in intensity and displacement in the peaks. The larger sketch of the shifting is presented. This shift in the peak changes the ionic radii of Sr ions to 1.12 Å and ionic radii of Cr are 0.615 Å, as well as ion replacement on the sub lattices A & B. By means of a consequence, the internal lattice strain produced by the loss in lattice properties caused by an increase in the dopant’s ratio precludes the formation of crystals. Because the c/a ratio is in the 2.32-2.44 range, the synthesized material belongs to the R-type hexagonal ferrites as shown in Table 2.

Table 2. Comparisons of unit volume cell (V), c/a ratio, x-ray density (dx) and molecular weights (M.W), bond length (B.L), and positional parameter (U) with Concentration x.

Concentration (x)	c/a	V (Å^3)	d_x (g/cm^3)	M.W	B.L (Å)	U	S.f
0.00	2.39	395.5	15.56	617.76	6.93	0.0582	0.477
0.02	2.32	391.4	15.71	617.04	6.78	0.0616	0.478
0.06	2.33	397.6	15.43	615.62	6.83	0.0611	0.479
0.1	2.44	378.6	16.16	614.19	6.91	0.0560	0.458

As replacement increased, cell unit volume decreased from 395.5Å^3 to 378.6Å^3 as given in Table 2. This volume reduction is justified due to the doping ions' differing ionic radii from the host. The volume deviation demonstrated that the cations had been properly replaced at the correct spot. Crystallites of diameters ranging from 7.00nm to 11.56nm were formed by the synthesized chemical [37].

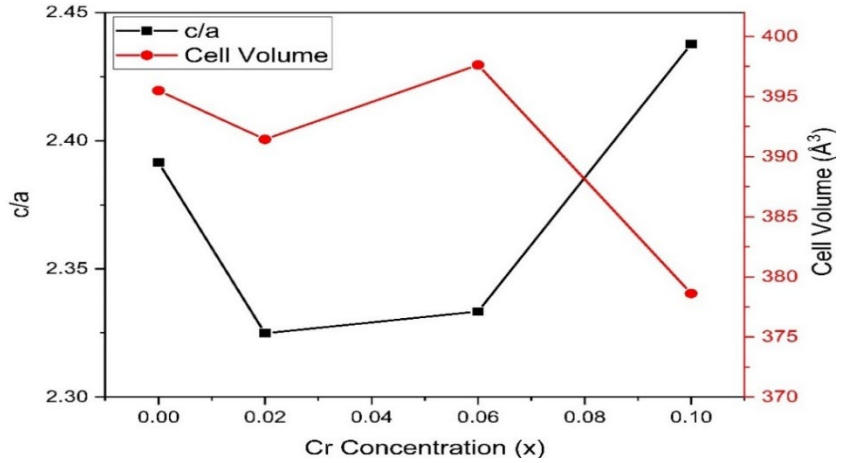

Fig. 4. Graph between concentration vs Cell volume and c/a

X-ray density of generated materials was calculated using equations.

$$d_{X-ray} = \frac{Z.M}{NA.\ V} \tag{4}$$

where V is the volume, NA is Avogadro's number; M is molar mass and $Z\ is\ 6$ for R-type hexaferrites [38]. The changes in X-ray density of the synthesized material due to the substitution are presented in Table 2. It was discovered that as the Sr-Cr ratio grew, the X-ray density increase up to $x = 0.02$ and formerlyreduction at $x = 0.06$ but at higher value of x its value increases. The reduced molecular weight of the replacement ions in contrast to the host explains this behavior. The cell volume, lattice constant and x-ray density have all dropped, as predicted by the hypothesis.

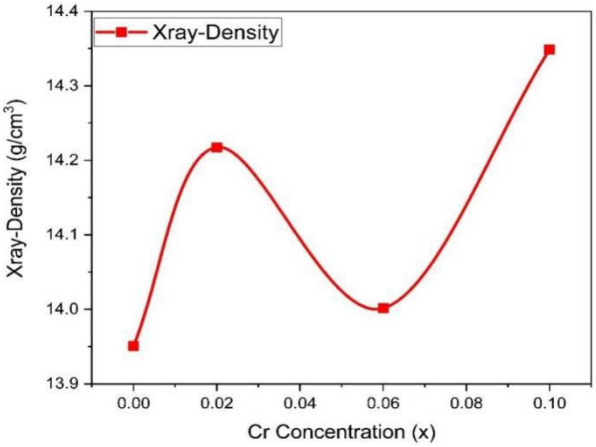

Fig. 5. Graph of bulk density-rays density and porosity.

In a crystal lattice, the "bond length" refers to the distance between the nuclei of two atoms that are bonded together within the crystal structure. It represents the equilibrium separation between atoms in a crystal lattice, where the attractive and repulsive forces between the atoms are balanced. The relation (5) determines the bond length of R- typed hexagonal ferrites

$$B.L = \sqrt{\frac{a^2}{3} + \left(\frac{1}{2} - u\right)^2 * c^2} \tag{5}$$

where “a” and “c” stand lattice parameters. In a hexagonal crystal lattice, the variable "u" in above equation represents a positional parameter used to describe the position of atoms or ions along the crystallographic axis "b" in the hexagonal unit cell. The specific formula used to calculate this positional parameter "u" for hexagonal crystal structures is

$$u = \frac{a^2}{3c^2 + 0.25} \tag{7}$$

where, "a" represents the lattice parameter, symbolic the length along one of the hexagonal axes, "c" is the lattice parameter, representing the length alongside the vertical axis and "u" is the positional parameter along the hexagonal "b" axis [39].

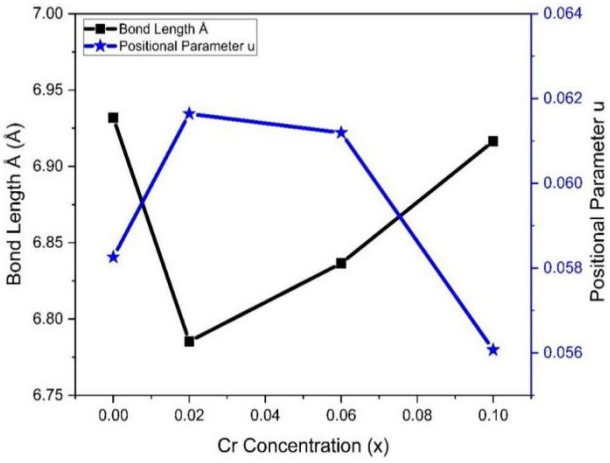

Fig. 6. Graph between concentration vs Bond Length and u.

The computed bond length values are provided in table 2 aimed at all the samples. It's evident formerly the table that decrease in bond length up to $x = 0.02$ as a result of the Cr content substitution, and these values align well with the lattice parameter values. But as the concentration of Chromium increases the bond length value also increase. Therefore, it can be affirmed after the preceding conversation that the introduction of Cr ions into uncontaminated ferrites led to alterations in the structural factors of uncontaminated ferrites. The smaller ionic radius of Cr ions resulted in an increasing in the bond length between ions, subsequently leading to a reduction in the unit cell volume for all the substituted samples. The computation of stacking faults in the produced nanoparticles is accomplished using the following equation:

$$S.f = \frac{2\pi^2}{45\sqrt{3.Tan\theta}} \tag{7}$$

Stacking faults are planar imperfections within the crystal lattice, and they often occur during the formation of crystals in relatively dense systems. The measured values of SF are illustrated in the table 2. In a series of samples denoted as $Sr_{1-x}Cr_xZn_2Fe_4O_{11}$ ($x = 0.00,0.02,0.06,0.1$) R-Type Hexaferrites the behavior of stacking faults exhibits unpredictability in relation to the chromium (Cr) content.

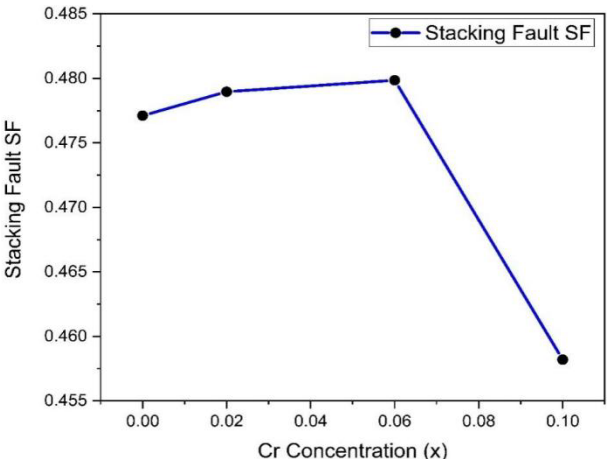

Fig. 7. Graph between concentration vs Stacking Fault.

Figure 7 illustrates that the stacking fault falls within the range of 0.458 to 0.479. Upon the introduction of Cr, there is an increase in stacking fault values (for x > 0.02–0.06). However, with further increases in Cr content (x = 0.1), the stacking fault once again decreases, as depicted in Figure 7. This observed variation may be influenced by the annealing temperature, leading to this heterogeneous behavior [40]. The extent to which the lattice is distorted due to the incorrect placement of an atom within its structure is referred to as the degree of lattice deformation. This degree of deformation can be quantified using the given equation [41].

$$R = \frac{2a\sqrt{\frac{2}{3}}}{c} \tag{8}$$

where the symbol "R" represents the measure of distortion. The graphical Illustration of the Lattice deformation is revealed in figure 8

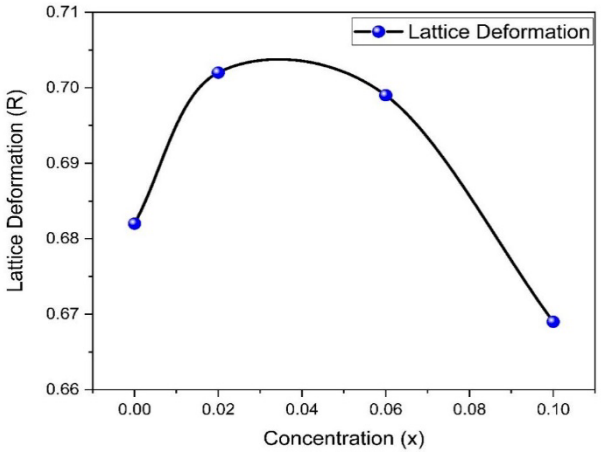

Fig. 8. Graph between concentration vs Lattice Deformation.

Number of Unit cell is calculated by using the given equation (9).

$$n = 0.6043 * \frac{D^3}{a^2 c} \tag{9}$$

The particle volume measured from relation in equation (10)

$$V = \frac{4\pi}{3} * \frac{D^3}{2} \tag{10}$$

Table 3. Comparison of Stacking Fault S.F with Concentration x.

Concentration (X)	**Crystallite Size (nm)**	**No. of Unit Cell**	**Volume of particles (A°)**
0.00	7.00	0.45	179.86
0.02	10.76	1.66	652.61
0.06	11.03	1.76	703.55
0.1	11.56	2.13	808.73

The evident in Table 3 and Figure 9 shows that particle size, number of unit cells and volume of particles follow similar styles. These parameters show a gradual sudden increase, and eventually stabilize. This behavior is attributed to the factor that the samples contain elements by different ionic radii, as indicated by their composition [40].

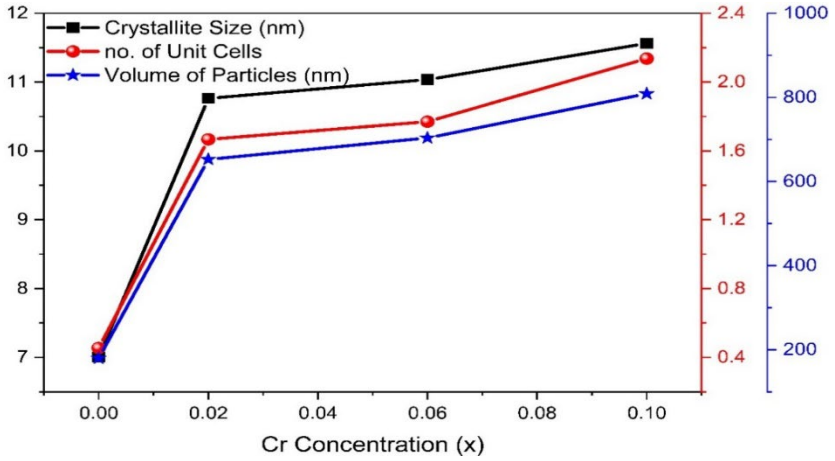

Fig. 9. Graph between concentration vs Crystallite size, number of unit cells& volume of particles.

3.2. FTIR analysis

FTIR analysis has been carried out to identify the functional groups of $Sr_{1-x}Cr_xZn_2Fe_4O_{11}$. The outcomes of FTIR spectra have been displayed in the figure 1. The band spectrum arises in the range of 400cm^{-1} to 480cm^{-1}. The band at 407cm^{-1} is due to stretching vibrations in Fe-o bonds. The bands at 436 cm^{-1} and 447 cm^{-1} are due to stretching vibrations of metal oxides ions. The band at 465 cm^{-1} is because of the metal-o-metal (M-o-M) vibrations. This M-o-M may contain the Sr-o-Sr, Cr-o-Cr, and Fe-o-Fe bonds. The band observed at 475 cm^{-1} stands to the o-H bond vibration [41].

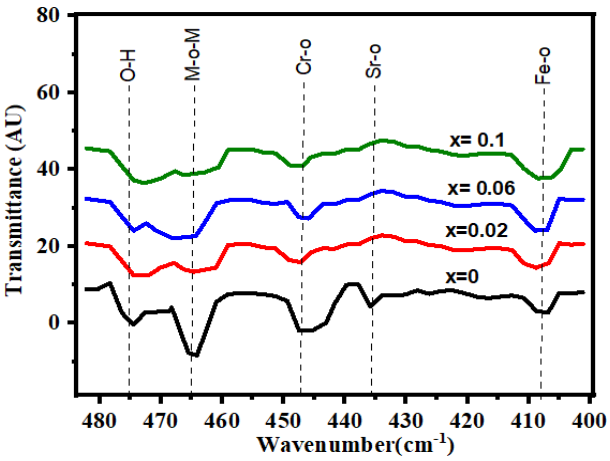

Fig 10. FTIR analysis of $Sr_{1-x}Cr_xZn_2Fe_4O_{11}$ R-Type Hexaferrites.

3.3. Surface morphology

The SEM imaginings were utilized to examine the dimensions, shapes, and distribution of particle sizes in R-Type Hexaferrites $Sr_{1-x}Cr_xZn_2Fe_4O_{11}$ (x=0.00, 0.02, 0.06, 0.1). Figures 11(a-d) presents the scanning electron microscope (SEM) images of R-Type Hexaferrites $Sr_{1-x}Cr_xZn_2Fe_4O_{11}$ (x=0.00, 0.02, 0.06, 0.1). At a 10um scale. The microstructure images of R-Type Hexaferrites $Sr_{1-x}Cr_xZn_2Fe_4O_{11}$ (x=0.00, 0.02, 0.06, 0.1) exhibit irregularly shaped particles with varying sizes. Micrographs confirm that the majority of nanoparticles are smaller than 30 nm, and there is a noticeable distinction between the sizes of doped and un-doped particles. Furthermore, the particle size increases as per the concentration of chromium rises. Here are the SEM Images of all the replicas of the $Sr_{1-x}Cr_xZn_2Fe_4O_{11}$R Type Hexaferrites [42].

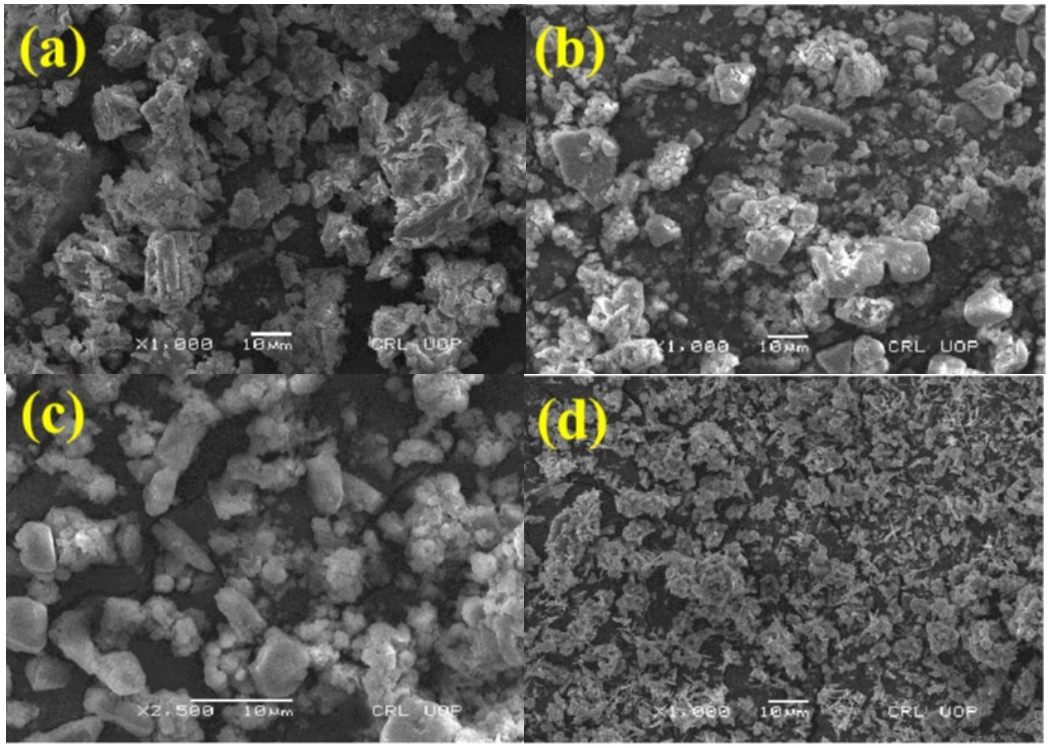

Fig. 11. (a-d): SEM Image of R-Type Hexaferrites.

3.4. Dielectric properties

The dielectric possessions all the samples of $Sr_{1-x}Cr_xZn_2Fe_4O_{11}$ (x=0.00, 0.02, 0.06, 0.1) have been evaluated at different frequencies ranging from 0 to 3 Giga Hz. All the samples have been tested at temperature of room. The computer controlled LCR-Hi-tech directly measured the different factorslike Dielectric constant (ε), AC conductivity (σac) and tangent loss (tan δ) of all the samples and depicted in the figures. The dielectric factors are calculated by using the following equations, Dielectric constant (ε′) of the models can be measured as [43].

$$\boldsymbol{\varepsilon' = \frac{Cd}{\varepsilon_0 A}} \quad (11)$$

$C = capacitance\ of\ parallel\ plate\ capacitor, A = \ the\ area\ of\ the\ pallet,$
$\varepsilon o = \ the\ permittivity\ of\ free\ space$. The dielectric tangent loss (δ) in terms of conductivity is:

$$tan\ \delta = 1/2\ \pi f C R \quad (12)$$

The equation (13) used to calculate the AC conductivity (σac) of all the samples on the base of loss tangent (tan δ) and dielectric constant (ε)

$$\sigma ac = 2\pi f \varepsilon 0\ \varepsilon'\ tan\ \delta \quad (13)$$

The dielectric constant (ε′) as the efficacy of the frequency has been depicted in the figure 12. It reflects those dielectric constant decreases by increasing the frequency. The dielectric constant of pure sample is minimum but as the concentration of Sr increases the dielectric constant also increases. The dielectric behavior could be understood by the Koop's theory. That theory explains the phenomenon of grains and grain boundary at different frequencies. At low frequencies the grain effects dominate in the crystallite. The grains are conducting at low frequency and the conduction and polarization mechanism occurs in the grain at low frequencies. The grain boundary is non-conducting at the low frequencies. The dielectric constant decreases when the frequency

rises because the grain boundaries effect starts at higher frequencies. The grain boundaries at greater frequency starts conduction mechanism as the charges accumulated on the grain boundaries starts vibrating with the frequency. The so much higher frequency makes the charges free because the charges do not response too fast as the change in frequencies. So, the charges show the unaffected behavior at higher frequency [44].

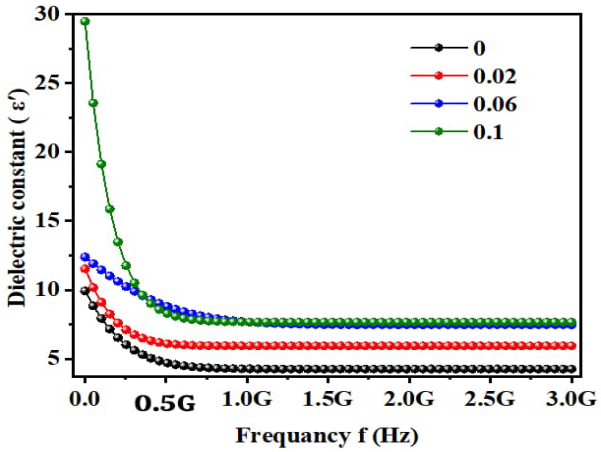

Fig. 12.The dielectric constant of all the as fabricated samples of $Sr_{1-x}Cr_xZn_2Fe_4O_{11}$ *(x=0.00, 0.02, 0.06, 0.1).*

The tangent loss of the as fabricated samples has been illustrated in figure 13. Behavior of dielectric loss might be clarified through Maxwell–Wagner polarization. This behavior may be effectively explicated through the concept given by Maxwell–Wagner polarization. This model says that the crystallite made up of two layers. One is grain and other is grain boundaries. It should be note that when frequency increases the tangent loss decreases. This behavior owes the conduction mechanism of the accumulated charges in the crystallite. At lower frequency the charges accumulate on the grain boundaries and a lot of energy required moving them to start the conduction mechanism. The so much dielectric losses arise in the crystallite. But at the higher frequency response the charges already vibrating with high frequency, so the very low energy can move them to start the conduction mechanism. This is the cause behind and the reducing performance of the dielectric loss of the prepared samples [45].

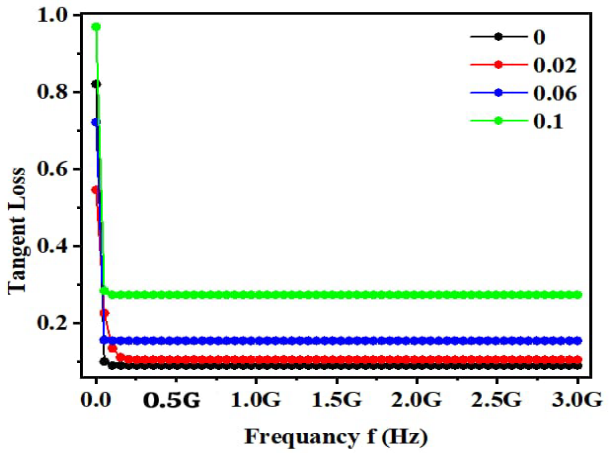

Fig. 13. Dielectric losses of all the samples of $Sr_{1-x}Cr_xZn_2Fe_4O_{11}$*(X=0.00, 0.02, 0.06, 0.1) with frequency changes.*

AC conductivity (σac) of the prepared samples has been shown in the figure 14. It shows that conductivity of all the samples increases by increasing the frequency. It is owing to the conduction of accumulated controls at grain boundary which are conducting at the higher frequency. The grain boundaries merged at higher frequency, as at the higher frequency the conduction mechanism arise. When the grain boundary and the grain merged the trapped charges at the grain boundaries become free to conduct the charges within the whole crystallite. The other reason is that the Sr has two valance electrons which contribute in the polarization and the conduction mechanism. The electro negativity of the Sr is lesser than the host Cr. In the result the Sr makes the weaker bonds than the Cr. These weaker bonds consume very low energy for bon breakage. When the frequency increased the weaker bonds cannot posse their strength to hold the bonding. This bond breakage contributes to the production a conduction of the free charges which increase the conductivity [46].

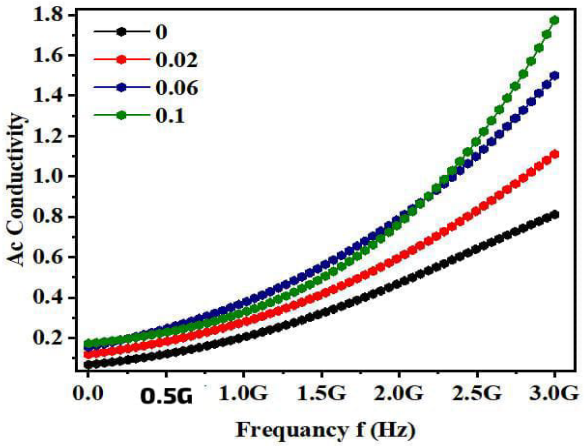

Fig. 14. The Ac conductivity of the as fabricated samples of $Sr_{1-x}Cr_xZn_2Fe_4O_{11}$ *(x=0.00, 0.02, 0.06, 0.1).*

The Q value determines the quality factors of the material. It can be calculated as:

$$Q = 1/\tan(\delta) \tag{14}$$

Higher the Q values represent high quality of material. The figure 15 shows the higher Q values as the Sr concentration increases. This is maybe due to the reduction in losses in the material [46].

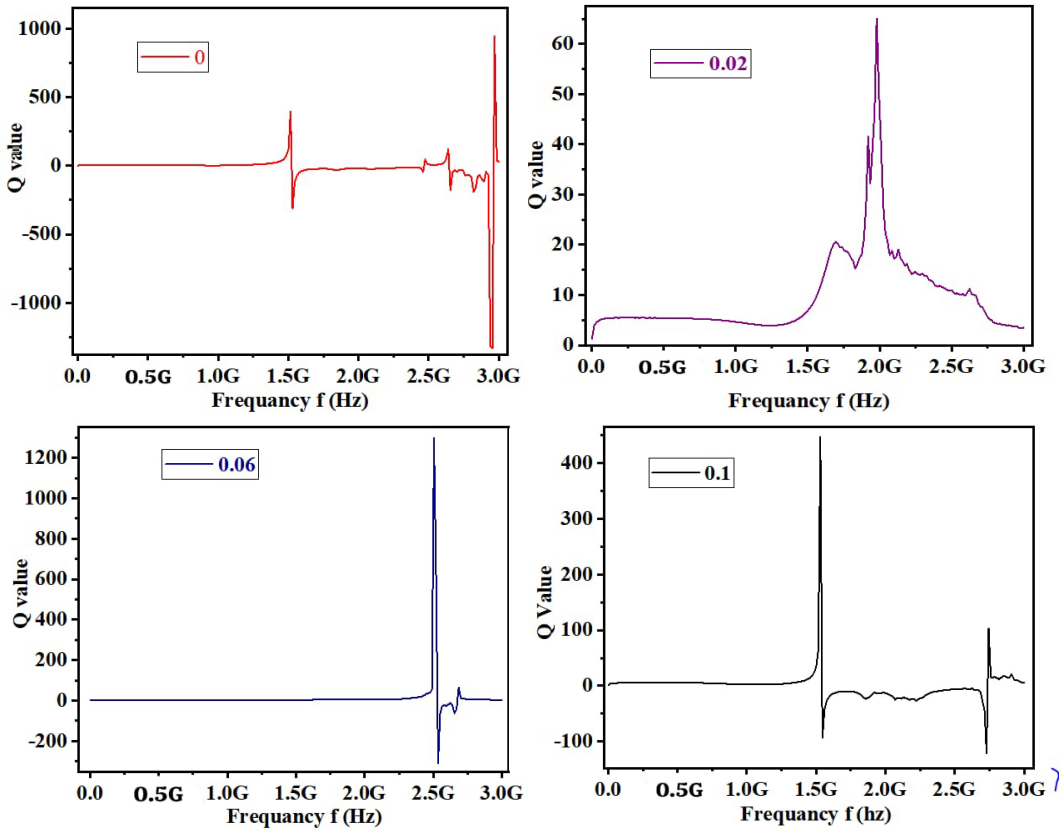

Fig. 15. The Q value of fabricated samples $Sr_{1-x}Cr_xZn_2Fe_4O_{11}$ at (X=0.00, 0.02, 0.06, 0.1).

4. Conclusion

The R-type hexagonal ferrites with formula $Sr_{1-x}Cr_xZn_2Fe_4O_{11}$ at x = (0.00, 0.02, 0.06, and 0.1) were synthesized by sol-gel auto combustion method and powder was annealed at about 950°C and finally we get the phase of hexagonal ferrites. Their crystalline size was measured by XRD and their grain size was 7 to 11.56 nm. Moreover, the interplanar spacing values of$Sr_{1-x}Cr_xZn_2Fe_4O_{11}$ show a decreasing trend as the Cr^{+2} content increases, ranging from 0.2897 Å to 0.28195 Å. This demonstrates the sensitivity of the material's lattice structure to changes in composition. The FTIR band spectra encompass frequencies between 400 cm^{-1} and 480 cm^{-1}. This range of spectral features indicates of specific chemical bonds and structural motifs within the material. SEM analysis of produced specimen's morphology revealed hexagonal grains like configuration. In that dominion the electrical properties exhibit fascinating behavior. It was observed that by increasing frequency, the dielectric constant decreases, which suggested that the material responses to applied electric field vary with frequency. Simultaneously, Moreover AC conductivity of material was increased with higher frequency, showing that the material becomes more conductive under these conditions. These results suggested that this frequency-dependent behavior can be essential in applications such as microwave devices and telecommunications, where tailored electrical properties are required.

Acknowledgements

The authors extend their appreciation to Taif University, Saudi Arabia for supporting this work through project number (TU-DSPP-2024-20).

References

[1] Gupta, T., Chauhan, C. C., Kagdi, A. R., Meena, S. S., Jotania, R. B., Singh, C., Basak, C. B. (2020), Ceramics International, 46(6), 8209-8226; https://doi.org/10.1016/j.ceramint.2019.12.049

[2] Chauhan, C. C., Gor, A., Gupta, T., Parmar, D. D., Jotania, R. B. (2024), Interactions, 245(1), 272; https://doi.org/10.1007/s10751-024-02113-7

[3] Moualhi, C., Horcheni, J., Moualhi, Y., Dachraoui, W., Bessais, L., Zouaoui, M. (2024), Materials Chemistry and Physics, 325, 129732; https://doi.org/10.1016/j.matchemphys.2024.129732

[4] Gupta, T., Chauhan, C. C., Kagdi, A. R., Meena, S. S., Jotania, R. B., Singh, C., Basak, C. B. (2020), Ceramics International, 46(6), 8209-8226; https://doi.org/10.1016/j.ceramint.2019.12.049

[5] Mahapatro, J., Meena, S. S., Agrawal, S. (2024), Journal of Rare Earths; https://doi.org/10.1016/j.jre.2024.01.010

[6] Mohammed, J., Batoo, K. M., Abdulaziz, A. S., Safana, A. S., Hafeez, H. Y., Raslan, E. H., Srivastava, A. K. (2021), Ceramics International, 47(13), 18455-18465; https://doi.org/10.1016/j.ceramint.2021.03.169

[7] Khan, M. A. (2024), Ceramics International; https://doi.org/10.1016/j.ceramint.2024.04.234

[8] Arshad, M., Khan, M. A., Rasool, R. T., Arshad, M. I., Albalawi, H., Abd-Rabboh, H. S., Jacob, J. (2023), Ceramics International, 49(12), 21036-21049; https://doi.org/10.1016/j.ceramint.2023.03.239

[9] Ibrahim, F. A., Ahmad, I., Hamdy, M. S., Solre, G. F., Asif, S. U. (2024), Inorganic Chemistry Communications, 113576; https://doi.org/10.1016/j.inoche.2024.113576

[10] Shidaye, M. N., Rehman, M., Abbas, Q., Abbas, S. K., Ramay, S. M., Shar, M. A., Atiq, S. (2023), Physica B: Condensed Matter, 666, 415125; https://doi.org/10.1016/j.physb.2023.415125

[11] Aleem, A., Khan, H. M., Zahid, M., Ouyang, C., Hajana, M. I., Azeem, W., Kebaili, I. (2024), Heliyon, 10(13); https://doi.org/10.1016/j.heliyon.2024.e33271

[12] Jasrotia, R., Prakash, J., Verma, R., Thakur, P., Kandwal, A., Wan, F., Thakur, A. (2023), Physica B: Condensed Matter, 415202; https://doi.org/10.1016/j.physb.2023.415202

[13] Ramirez, A. P. (1994), Annual Review of Materials Science, 24(1), 453-480; https://doi.org/10.1146/annurev.matsci.24.1.453

[14] Frandsen, B. A., & Fischer, H. E. (2024), Chemistry of Materials, 36(19), 9089-9106; https://doi.org/10.1021/acs.chemmater.4c01535

[15] Chauhan, C. C., Gor, A., Gupta, T., Parmar, D. D., Jotania, R. B. (2024), Interactions, 245(1), 272; https://doi.org/10.1007/s10751-024-02113-7

[16] Contreras-Valero, J. F., Gualtero-Trujillo, S. M., Cortés-Fraile, G. C., Hernández-Garzón, S., Manrique-Marín, N., Narváez-Chaves, M. Á., Valderrama-Beltrán, S. L. (2024), Heliyon, 10(13); https://doi.org/10.1016/j.heliyon.2024.e33698

[17] Amjad, T., Sadiq, I., Javaid, A. B., Riaz, S., Naseem, S., Nadeem, M. (2019), Journal of Alloys and Compounds, 770, 1112-1118; https://doi.org/10.1016/j.jallcom.2018.08.114

[18] Hussain, S., Sadiq, I., Khan, H. M., Idrees, M., Sadiq, F., Shah, A., Naseem, S. (2021); Physica B: Condensed Matter, 605, 412642. https://doi.org/10.1016/j.physb.2020.412642

[19] Idrees, M., Sadiq, I., Hussain, S., Sadiq, F., Javaid, M., Riaz, S., Naseem, S. (2021), Materials Science and Engineering: B, 273, 115435; https://doi.org/10.1016/j.mseb.2021.115435

[20] Shahbaz, M., Sadiq, I., Butt, M. M. H., Javaid, A. B., Idrees, M., Hussain, S., Khan, H. M. (2020), Journal of Magnetism and Magnetic Materials, 499, 166309; https://doi.org/10.1016/j.jmmm.2019.166309

[21] Arshad, M.I., Zahid, H., Sajjad, M.T., Amin, N., Thanh, N.T.K., Amami, M., Morley, N., Alresheedi, F., Dastgir, A., Siddeeg, S.M., Hasan, M.S., 2024, Powder Technology, 438, p.119469; https://doi.org/10.1016/j.powtec.2024.119469

[22] Hasan, M.S., Khan, M.I., Ali, S.S., Brahmia, A., 2024, Materials Science and Engineering:

B, 301, p.117180; https://doi.org/10.1016/j.mseb.2024.117180

[23] Hasan, M.S., Ali, S.S., Khan, M.I., Rizwan, M., Zulqarnain, M., Hussain, A., 2023, Materials Chemistry and Physics, 301, p.127538; https://doi.org/10.1016/j.matchemphys.2023.127538

[24] Hasan, M., Khan, M., Kanwal, S., Irfan, M., Al-Muhimeed, T.I., Mumtaz, S., 2022, Digest J. Nanomater. Biostruct, 17, pp.1527-1533; https://doi.org/10.15251/DJNB.2022.174.1527

[25] Farooq, W.A., SajjadUlHasan, M., Khan, M.I., Ashraf, A.R., Abdul Qayyum, M., Yaqub, N., Almutairi, M.A., Atif, M., Hanif, A., 2021, Molecules, 26(5), p.1399; https://doi.org/10.3390/molecules26051399

[26] Amin, N., Hasan, M.S.U., Majeed, Z., Latif, Z., unNabi, M.A., Mahmood, K., Ali, A., Mehmood, K., Fatima, M., Akhtar, M., Arshad, M.I., 2020, Ceramics International, 46(13), pp.20798-20809; https://doi.org/10.1016/j.ceramint.2020.05.079

[27] Akhtar, M., Hasan, M.S., Amin, N., Morley, N.A., Arshad, M.I., 2024, Journal of Rare Earths, 42(1), pp.137-146; https://doi.org/10.1016/j.jre.2023.01.021

[28] Fatima, M., Hasan, M.S.U., Akhtar, M., Morley, N., Amin, N., Rehman, A.U., Arshad, M.I., Amami, M., Yaqub, B., Ezzine, S., 2023, ACS omega, 8(44), pp.41169-41181; https://doi.org/10.1021/acsomega.3c03993

[29] Khan, Z., Khalid, A. D., Khan, M. I., Parveen, B., Moussa, I. M. (2024), Chalcogenide Letters, 21(11), 933-943; https://doi.org/10.15251/CL.2024.2111.933

[30] M.S. Hasan, S.S. Ali, M. Rizwan, M.I. Khan, H.M. NaeemUllah, Muhammad Imran Irfan, Journal of Alloys and Compounds, Volume 956, 2023, 70392; https://doi.org/10.1016/j.jallcom.2023.170392

[31] Dhage, V. N., Mane, M. L., Keche, A. P., Birajdar, C. T., Jadhav, K. M. (2011), Physica B: Condensed Matter, 406(4), 789-793; https://doi.org/10.1016/j.physb.2010.11.094

[32] Mohammed, I., Srivastava, A. K. (2024), Nanostructured Hexagonal Ferrites (pp. 99-116). Elsevier; https://doi.org/10.1016/B978-0-443-18537-3.00007-9

[33] Anjum, S., Sehar, F., Mustafa, Z., &Awan, M. S. (2018), Applied Physics A, 124, 1-11; https://doi.org/10.1007/s00339-017-1456-6

[34] Dhage, V. N., Mane, M. L., Babrekar, M. K., Kale, C. M., Jadhav, K. M. (2011), Journal of Alloys and Compounds, 509(12), 4394-4398; https://doi.org/10.1016/j.jallcom.2011.01.040

[35] Sharrouf, M., Awad, R., Habanjar, K. (2023), Applied Physics A, 129(11), 807; https://doi.org/10.1007/s00339-023-07079-x

[36] Rana, K., Thakur, P., Tomar, M., Gupta, V., Thakur, A. (2018), Ceramics International, 44(6), 6370-6375; https://doi.org/10.1016/j.ceramint.2018.01.028

[37] Ijaz, I., Arshad, R. H., Saeed, S., Sadiq, I., Sadiq, F., Idrees, M., Ahmad, F. (2024), Results in Surfaces and Interfaces, 17, 100298; https://doi.org/10.1016/j.rsurfi.2024.100298

[38] Naheed, F., Irfan, M., Gulbadan, S., Akhtar, M. N., Ashraf, G. A., Rasool, R. T., Khan, M. A. (2023), Materials Today Communications, 35, 106006; https://doi.org/10.1016/j.mtcomm.2023.106006

[39] Mosleh, Z., Kameli, P., Poorbaferani, A., Ranjbar, M., Salamati, H. (2016), Journal of Magnetism and Magnetic Materials, 397, 101-107; https://doi.org/10.1016/j.jmmm.2015.08.078

[40] Ali, I., Islam, M. U., Awan, M. S., Ahmad, M. (2013), Journal of Alloys and Compounds, 547, 118-125; https://doi.org/10.1016/j.jallcom.2012.08.122

[41] M.S. Hasan, M.I. Khan, Mongi Amami, A. Laref, BaoqingNie, Jian Liu, Inorganic Chemistry Communications, Volume 167, 2024, 112666; https://doi.org/10.1016/j.inoche.2024.112666

[42] M.I. Arshad, M.S. Hasan, Atta Ur Rehman, N. Amin, Le Duc Tung, N.T. Kim Thanh, N.A. Morley, Mongi Amami, Faisal Alresheedi, Safa Ezzine, M.A. Gadhi, Journal of Alloys and

Compounds, Volume 972, 2024, 172847;
https://doi.org/10.1016/j.jallcom.2023.172847

[43] Aslam, A., Islam, M. U., Ali, I., Awan, M. S., Irfan, M., Iftikhar, A. (2014). Ceramics International, 40(1), 155-162; https://doi.org/10.1016/j.ceramint.2013.05.116

[44] Muhammad Imran Arshad, M.S. Hasan, Atta Ur Rehman, Maria Akhtar, Le Duc Tung, N. Amin, Khalid Mahmood, Adnan Ali, ThithawatTrakoolwilaiwan, Nguyen Thi Kim Thanh, Ceramics International, volume 48, Issue 10, 2022, Pages 14246-14260;
https://doi.org/10.1016/j.ceramint.2022.01.313

[45] Mujtaba, A., Khan, M.I., Hasan, M.S., Ali, S.S., Shahid, W., Fatima, M., Abd-Rabboh, H.S., Alwadai, N., 2023, Journal of Materials Research and Technology, 23, pp.4538-4550;
https://doi.org/10.1016/j.jmrt.2023.02.038

[46] Lodhi, M. Y., Khan, M. A., Majeed, A., Alharthi, S., Amin, M. A., Boukhris, I. (2022), Ceramics International, 48(6), 8612-8619;
https://doi.org/10.1016/j.ceramint.2021.12.072